Full length article

Electrochemical shock and transverse cracking in solid electrolytes

Yin Zhang [a], Yanhao Dong [b,*], Ju Li [c,d,*]

[a] *Department of Mechanics and Engineering Science, College of Engineering, Peking University, Beijing, 100871, China*
[b] *State Key Laboratory of New Ceramics and Fine Processing, School of Materials Science and Engineering, Tsinghua University, Beijing, 100084, China*
[c] *Department of Nuclear Science and Engineering, Massachusetts Institute of Technology, Cambridge, MA, 02139, USA*
[d] *Department of Materials Science and Engineering, Massachusetts Institute of Technology, Cambridge, MA, 02139, USA*

ARTICLE INFO

ABSTRACT

Ceramic solid electrolytes are crucial for electrochemical devices, including emerging solid-state batteries. However, they are susceptible to degradation and failure under harsh conditions, leading to dendrite growth, cracking and short circuits. While longitudinal lithium dendrites have been identified as a primary degradation mechanism, recent experiments have revealed transverse reduction fronts and bowl-shaped cracks that differ significantly from the longitudinal picture. We propose an electrochemical shock model to explain these transverse degradation modes in solid electrolytes (SE) and mixed ionic-electronic conductors (MIEC), where SE is taken to be the very weakly electronic leaking limit of MIEC. The model describes a transverse layer with an abrupt oxygen potential jump over a short distance, caused by the electronic transport bottleneck on the Brouwer diagram. Using $Li_7La_3Zr_2O_{12}$ as an example, we demonstrate that even minor nonuniform lithium distribution associated with an electrochemical shock can induce stress concentrations, resulting in electrolyte cracking and bowl-shaped cracks. The electrochemical shock model highlights the significance of finite electronic conductivity in the degradation of SE and MIEC, providing insights for the design of durable solid electrolytes.

1. Introduction

Li-ion batteries (LIBs) have emerged as the main power sources for portable electronics and electric vehicles, due to their remarkable energy density and extended lifespan [1–3]. In the pursuit of a successful battery desired for electric vehicles, solid-state Li metal batteries (SSLMBs) are believed to be one of the most promising candidates [4,5]. For example, lithium metal anode, high-voltage cathode NMC, and ceramic electrolytes of garnet $Li_7La_3Zr_2O_{12}$ (LLZO, doped with Ta, Ga, Al, etc. to stabilize the cubic phase) [6–8] can achieve high energy density, high power density and wide operating temperature [9]. In addition, the solid electrolytes (SEs) with high mechanical strength are believed to impede the lithium dendrite growth, therefore significantly lowering the risk of short-circuiting and combustion compared to the conventional liquid organic electrolytes. However, under high voltage or repeated charge-discharge cycles, Li dendrite growth could still happen and cause cracking and failure in SEs at 0.5 mA cm^{-2} for doped-LLZO [10,11], which is much lower than the critical current density of 10 mA cm^{-2} in liquid electrolytes [12]. Thus, such contradiction with the conventional belief warrants a mechanistic understanding of the possible mechanisms of crack initiation in SEs.

Recently, Hao et al. [13] used in-situ synchrotron X-ray computed tomography (XCT) to track crack propagation and lithium penetration process in Li_3PS_4 solid electrolyte, as shown in Fig. 1a. They found that the cracks are only partially filled with Li metal so that the cell can continue to operate even after the cracks reach the cathode side. Ning et al. [14,15] visualized the crack propagation and Li metal ingress in Li_6PS_5Cl with in-situ XCT. They observed that the crack initiated predominantly with spallation near the surface with the electrode edge, as shown in Fig. 1b. Zhao et al. [16] conducted an in-situ observation of Li deposition-induced cracking in garnet $Li_{6.4}La_3Zr_{1.4}Ta_{0.6}O_{12}$, where the crack initiated underneath the Pt electrode, forming a bowl-shaped crack with partially filled Li metal, as shown in Fig. 1c. There are two degradation modes observed in these experiments: longitudinal cracks parallel to the current density direction, and transverse cracks perpendicular to the current density. The longitudinal cracks could be attributed to the lithium dendrite, as the dendrite tends to grow towards the opposite electrode, leading to cracks parallel to the current density. However, the physical origin of transverse cracks remains elusive.

From the modeling perspective, the cracks initiation and propagations in ceramic electrolytes are mainly investigated as pressurized cracks [17–19] and dislocation climb [20], where the pressure from Li

---

* Corresponding authors.
  E-mail addresses: dongyanhao@tsinghua.edu.cn (Y. Dong), liju@mit.edu (J. Li).

insertion dendrite provides the major thermodynamic driving force of crack formation. Since Li metals have a low yield strength of around 1 MPa [21], the crack must be filled by Li to produce high enough pressure for crack propagation, which contradicts experimental observations of partially filled Li in transverse cracks [13,14,16]. These models, although suitable for longitudinal cracks, cannot explain the transverse cracks partially filled with Li dendrite.

On the other hand, Dong et al. [22,23] have studied the sharp potential jump in mixed conducting oxide electrolytes under the assumption of steady-state transport and local equilibrium [24]. In this model, the sharp oxygen potential jump originates from the p-type/n-type transition of electronic conductivity inside mixed conducting electrolytes, which leads to nonuniform grain growth with dramatic grain size transition halfway across the electrolyte thickness [25] at high temperatures under processing conditions. The same model could be applied to the LIB system due to the very weakly mixed conducting nature of solid electrolytes [26,27]. In our framework, solid electrolyte (SE) is regarded as the very weakly electronically conducting ($t_{\text{electronic}} \rightarrow 0$) limit of the general class of mixed ionic-electronic conductors (MIEC), where $t_{\text{electronic}}$ is the electronic transference number, proportional to the electron/hole concentrations on the Brouwer diagram times the electronic mobility. Vice versa, metals (M) is regarded as the very weakly ionically conducting limit ($t_{\text{electronic}} \rightarrow 1$) of MIEC, as there are also well-known metallic oxides, borides and nitrides. For a SSLMB to function well, it must have a SE separator with rather low $<t_{\text{electronic}}>$. For example, the users may require 1 hour to charge SSLMB more or less fully (by ionic conduction across SE), but 12 months to hold its charge (electronic leakage), then this would require an average electronic transference number $<t_{\text{electronic}}> \leqslant 1/(24 \times 365) \approx 10^{-4}$. We note that while 10^{-4} is tiny, it is not absolutely zero, especially considering the shelf life of a rechargeable battery is required to be a decade or more, and it needs to survive hundreds to thousands of cycles, so minute electronic leakage over the long term can still leave significant impact on the SE, given that electronic voltage as high as 4 Volt is sustained across the SE separator that is only tens of microns thick, approaching MV/m electric field.

Given the importance of $t_{\text{electronic}}$, we note however $t_{\text{electronic}}$ is not an intrinsic property of the ceramic phase only, and depends on external conditions such as doping and PO_2 that affect its non-stoichiometry, and can thus vary spatially even within the same phase. It is well known from textbook Brouwer diagrams that as one sweeps the oxygen potential $\log PO_2$ from reducing (low U, where $\mu_{\text{e}^-} \propto -eU$ is the electronic chemical potential) to oxidizing (high U), $t_{\text{electronic}}$ will become more dominant on both the very reducing and the very oxidizing ends (assuming phase stability is guaranteed), so a solid electrolyte will become relatively more "leaky" of electrons at both low and high U's, even when U is still within the phase's electrochemical voltage stability window. There is also a particular "intrinsic" value of $\log PO_2$ / μ_{e^-} / U for any SE-like phase, where $t_{\text{electronic}}$ is minimized on the log scale, aka the electronic transport bottleneck, and this observation is generally true irrespective of the absolute magnitudes of the electron/hole concentrations relative to the ionic carrier concentrations. As the SE separator in a SSLMB is by definition sandwiched between a high-U oxidizing MIEC (the positive) electrode and a low-U reducing (the Li-metal) electrode, this electronic transport bottleneck will be experienced somewhere in the middle of the SE, where a very large *gradient* is needed to maintain steady-state electronic leakage (for if the small but finite electronic leakage flux is *not* maintained at steady state in SE, there will be finite electronic flux divergence and associated Faradaic reactions, and the SE will decompose electrochemically over long-term operations, which is not what we want in SSLMB). But even without Faradaic decompositions inside the SE, this large $\log PO_2$ / μ_{e^-} / U gradient associated with the intrinsic electronic bottleneck can still drive mechanical damage, since the $t_{\text{electronic}}$ minimum is quite deep (two straight lines crossover on log-scale), and so the magnitude of the peak gradient is exponentially large, behaving like a spatial singularity front, i.e. "electrochemical shock" in our title. The electrochemical model could be combined with the eigenstrain method to solve the internal stress field from Li-insertion-induced volume expansion. Here, we propose a theoretical model of mechanical stress generated from the electronic conductivity bottleneck. This model can explain the bowl-shaped crack observed in LLZO SEs shown in Fig. 1d, and provide design principles for future solid-state electrolytes. The framework outlined in this paper is also applicable to explaining mechanical damage in general MIECs, for example the cathode oxides like LiCoO_2 (LCO), LiNi_{0.8}Co_{0.15}Al_{0.05}O_2 (NCA) and LiNi_{0.8}Mn_{0.1}Co_{0.1}O_2 (NMC) materials used in SSLMBs and LIBs, as well as certain forms of interfacial damage between MIEC/SE, MIEC/M and MIEC/MIEC.

(a)

(b)

(c)

(d)
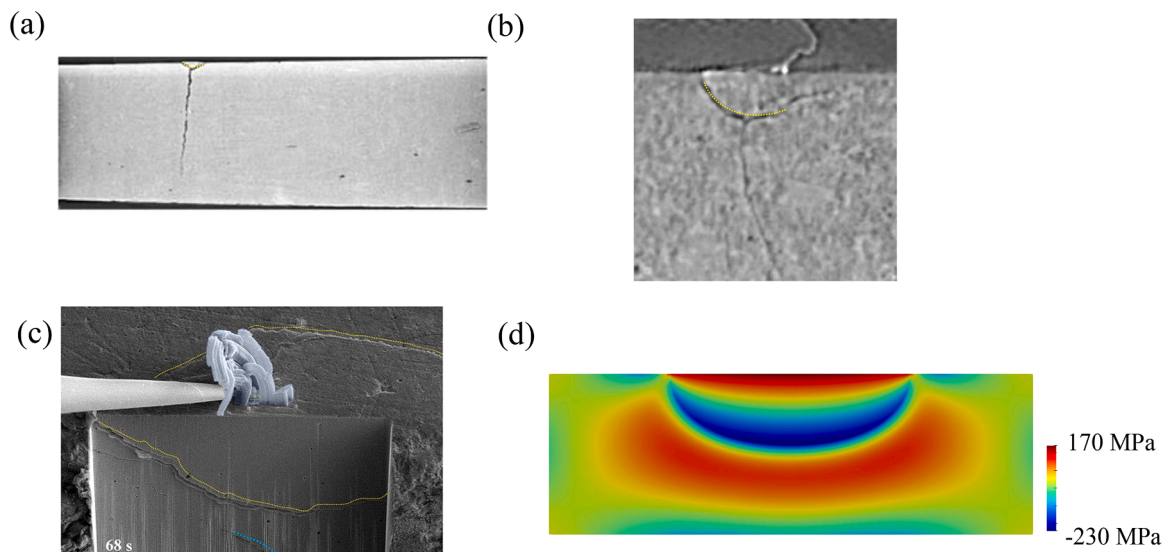
Fig. 1. (a) Crack initiation in Li_3PS_4 observed by XCT. Reproduced with permission from ref [13]. Copyright 2021 Elseiver Ltd. (b) XCT scan of a spallation at the edge of the lithium electrode, and a vertical crack under the spallation. Reproduced with permission from ref [14]. Copyright 2021 Springer Nature. (c) Formation of a bowl-shaped crack in LLZO. Reproduced with permission from [16]. Copyright 2022 John Wiley Sons Inc. (d) Pressure field predicted from our chemo-mechanical model, showing a bowl-shaped high-stress region.

2. Origin of transport-induced electrochemical shock and internal stress

To understand transport bottlenecks in solid electrolytes, we use LLZO as a prototypical solid electrolyte with mixed ionic and electronic conduction, but just with very low $t_{\text{electronic}}$ magnitude under normal conditions. Here, we only consider the motion of Li^+ ions and electrons owing to the limited mobilities of other species (La^{3+}, Zr^{4+}, Ta^{5+}, and O^{2-}) at room temperature. We assume the local equilibrium of the following two reactions,

$$Li^+ + e^- = Li^0 \tag{1}$$

$$e^- + h^+ = nil \tag{2}$$

The first equation assumes that a mobile Li^+ ion can capture an excess electron (conduction-band-minimum Bloch wavefunction, forming a Gaussian wave pack) to constitute a hypothetical immobile particle, the nominal Li^0(LLZO) species. The use of Li^0(LLZO) species and its chemical potential $\widetilde{\mu}_{Li^0}$ is exactly analogous to the use of O_2(LLZO) species and PO_2 for thermodynamic discussions (e.g. textbook Brouwer diagrams). Since some popular halide and sulfide SEs do not have oxygen inside, but must have lithium to support lithium-ion conductivity, using Li^0(LLZO),$\widetilde{\mu}_{Li^0}$ notation is just more natural, with $\widetilde{\mu}_{Li^0}$ correlating as $-(k_B T \log PO_2)/4$ in the case of oxide SEs for Brouwer diagram. These two reversible reactions in dynamic equilibrium are equivalent to the electrochemical potential equilibrium,

$$\widetilde{\mu}_{Li^+} + \widetilde{\mu}_{e^-} = \widetilde{\mu}_{Li^0} \tag{3}$$

$$\widetilde{\mu}_{e^-} + \widetilde{\mu}_{h^+} = 0 \tag{4}$$

In this paper, we use the symbol μ_{R^q} to represent the chemical potential of species R^q with the charge of q, and $\widetilde{\mu}_{R^q} = \mu_{R^q} + q\phi$ to denote the electrochemical potential, including the electrostatic potential term $q\phi$. The electrochemical potential is defined as free energy per particle in the unit of electron-volt. The chemical potential of electrons and holes could be determined with respect to its concentration under the dilute limit. For example,$\mu_{e^-} = \mu_{e^-}^{ref} + k_B T \ln(c_{e^-}/c_{e^-}^{ref})$, $c_{e^-}^{ref}$ and $\mu_{e^-}^{ref}$ are the reference concentration and chemical potential of electrons.

Here we want to elaborate a bit on the physical meaning of "Li^0(LLZO)" and $\widetilde{\mu}_{Li^0}$ in LLZO, because these notations are not very often seen in the context of the oxide bulk phase. We first note that a nominal line-compound phase such as garnet $Li_7La_3Zr_2O_{12}$ still has a finite (but minuscule) solubility range, that is, $Li_{7-\delta}La_3Zr_2O_{12}$ may stay as a globally stable single phase within a finite range of δ, according to the Gibbs phase rule. This is just like any binary intermetallic compound $A_{7-\delta}B$ with A=Li and B=$La_3Zr_2O_{12}$. Granted, the single-phase stability range of $\delta \in [\delta^{lower}, \delta^{upper}]$ is tiny, because the Gibbs free energy varies violently with δ for line compound phases (needle-shaped molar Gibbs free energy $g(X)$, where X is the pseudo-binary composition), and as a result, so does the chemical potential μ_A, according to the tangent extrapolation rule for obtaining $\mu_A(X)$ from $g(X)$. In such a pseudo-binary chemical free energy plot, there is a finite range of $\mu_A \in [\mu_A^{lower}, \mu_A^{upper}]$ that can be called the stability window of the line compound, beyond which the line compound will decompose, i.e. the A-B system will fall in two-phase regions. Because of the violent slopes of $\mu_A(X)$versus X, or δ, the corresponding single-phase stability range of $\delta \in [\delta^{lower}, \delta^{upper}]$ may be small, but nonetheless $[\delta^{lower}, \delta^{upper}]$ is finite, and more importantly, all the physical properties such as the lattice stress-free strain, and the magnitudes and character of the mixed conductivities, depend on δ sensitively. Since we have identified A as Li or "Li^0(LLZO)", it is in this thermodynamic marginal-cost sense that we identify $\mu_A \equiv \mu_{Li^0}$. Thus, slightly larger δ means more reduced LLZO, and slightly lower δ means more oxidized LLZO. It is obvious to practitioners that beyond certain limits, LLZO can be reductively decomposed, or oxidatively decomposed, which corresponds to the electrochemical stability window of

this solid electrolyte. Here Li^0(LLZO) can be thought of as a composite particle of Li^+ bound to an excess electron, all living in the LLZO structure. It does not mean a metallic lithium atom, and certainly does not mean metallic lithium atoms in the BCC phase. The "electrochemical shock" in the paper title is in fact a narrow region of transition between quite reduced LLZO and quite oxidized LLZO, with a self-developed eigen-strain mismatch (according to the Vegard's law) significant enough that can cause brittle fracture, since it does not take much elastic strain in ceramics to cause fracture.

The charged species could form drift current by external electrostatic field and diffusion current by chemical potential gradient. We combine these two terms and write the current density $\mathbf{j}_R$ for each charged specie R in terms of its electrochemical potential $\widetilde{\mu}_R$ and conductivity σ_R as following,

$$\mathbf{j}_{Li^+} = -\frac{\sigma_{Li^+}}{e}\nabla\widetilde{\mu}_{Li^+} \tag{5}$$

$$\mathbf{j}_{e^-} = \frac{\sigma_{e^-}}{e}\nabla\widetilde{\mu}_{e^-} \tag{6}$$

$$\mathbf{j}_{h^+} = -\frac{\sigma_{h^+}}{e}\nabla\widetilde{\mu}_{h^+} = \frac{\sigma_{h^+}}{e}\nabla\widetilde{\mu}_{e^-} \tag{7}$$

where e is the charge of one electron. Then the total current density is expressed as the sum of Li ion current, electrons and holes current $\mathbf{j}_{charge} = \mathbf{j}_{Li^+} + \mathbf{j}_{e^-} + \mathbf{j}_{h^+}$. Here we assume that the neutral Li atom / Li^0(LLZO) is immobile, therefore the Li ion flow is related to the Li mass flow by,

$$\mathbf{J}_{Li} = \frac{\mathbf{j}_{Li^+}}{e} = -\frac{\sigma_{Li^+}}{e^2}\nabla\widetilde{\mu}_{Li^+}. \tag{8}$$

The assumption that Li^0(LLZO) does not generate a mass flux contribution in response to the compositional spatial gradient $\nabla\delta$ can be relaxed and modeled in later work. At a steady state, the concentration field remains time-independent and charge neutrality is enforced everywhere in the SE. Thus, the current density of all charged species and the Li mass flow should both be divergence-free,

$$\nabla\cdot\mathbf{j}_{charge} = 0 \tag{9}$$

$$\nabla\cdot\mathbf{J}_{Li} = 0 \tag{10}$$

The conductivity of each species is assumed to be proportional to its concentration and mobility. In the practical batteries, the Li ion concentration is almost constant across the SE as measured by experiments. Thus, the ionic conductivity of Li ion can be assumed constant throughout the simulations. This assumption does not imply that the total Li concentration (Li^+ and Li^0) is constant across the SE, because the concentration of Li^0 could be a non-uniform distribution as the SE could exchange Li with contacting electrodes. On the other hand, the electric conductivity could vary by many orders of magnitude due to the concentration change of electrons and holes. Their conductivities can be expressed in terms of their chemical potential and mobility M from standard defect chemistry [28].

$$\sigma_{e^-} = ec_{e^-}M_{e^-} = eM_{e^-}\exp\left(-\frac{\mu_{e^-}}{k_B T}\right) \tag{11}$$

$$\sigma_{h^+} = ec_{h^+}M_{h^+} = eM_{h^+}\exp\left(-\frac{\mu_{h^+}}{k_B T}\right) = eM_{h^+}\exp\left(\frac{\mu_{e^-}}{k_B T}\right) \tag{12}$$

These exponential dependencies lead to highly nonuniform conductivity spanning over many orders of magnitudes. A steady state for 1D case could be achieved by the following thought experiment. Initially, the Li^+ ion is constant and uniform across the SE. The reactions of Eqs. (1) and (2) reach local equilibrium as the external electric potential biased the electrochemical potential, resulting in a nonuniform and nonlinear distribution of electrons and holes. The conversion from

Li$^+$ ions to Li^0 happens first in the area with a high electron concentration. This conversion leads to local Li$^+$ ion shortage, making it possible to transport Li$^+$ ions from the external electrodes. This process effectively changes the composition of LLZO marginally and transport Li atom from electrodes to Li^0 in the SE. This redistribution of off-stoichiometry δ, e.g. Li$_{7-\delta}$La$_3$Zr$_2$O$_{12}$ due to finite divergence of electronic flux $\nabla\cdot(\mathbf{j}_{e^-}+\mathbf{j}_{h^+})=-\nabla\cdot\mathbf{j}_{Li^+}\neq 0$ is a form of Faradaic reactions, which can take place inside a stable single MIEC phase within a finite range of δ, but the divergence can also drive phase transformation of the solid if δ exceeds the stability range $[\delta^{lower}, \delta^{upper}]$ of this phase, which is certainly not what we want for long-term stable operations of the SSLMB.

The transport bottleneck of electron-hole conductivity will lead to the heterogeneous distribution of marginal Li^0(LLZO), similar to a shock front. Note that it does not take much Li^0(LLZO) marginal atoms to cause drastic physical properties changes in Li$_{7-\delta}$La$_3$Zr$_2$O$_{12}$ as this chemical system is "stiff", changing it from "much reduced LLZO" to "much oxidized LLZO". Since the excess storage of Li atom introduces the volume expansion, we can determine the stress distribution inside SEs by the eigenstrain method. The elastic strain $\boldsymbol{\varepsilon}^e$ can be determined by the total strain minus the volume expansion eigenstrain $\boldsymbol{\varepsilon}^*$ related to the Li atom concentration,

$$\boldsymbol{\varepsilon}^{\mathrm{e}} = \frac{1}{2}\left[\nabla\mathbf{u}+(\nabla\mathbf{u})^{\mathrm{T}}\right] - \boldsymbol{\varepsilon}^* \tag{13}$$

$$\boldsymbol{\varepsilon}^* = \alpha\left(c_{Li^0}-c_{Li^0}^{\mathrm{ref}}\right)\mathbf{I} = \alpha c_{Li^0}^{\mathrm{ref}}\left[\exp\left(\frac{\mu_{Li^0}-\mu_{Li^0}^{\mathrm{ref}}}{k_B T}\right)-1\right]\mathbf{I} \tag{14}$$

$c_{Li^0}^{\mathrm{ref}}$ and $\mu_{Li^0}^{\mathrm{ref}}$ are the concentration and chemical potential of Li^0 atom at the reference state 1.48V, α is the partial molar volume of the Li^0 atom. The magnitude of the α is calculated from density functional calculations. We determined this parameter $c_{Li^0}^{\mathrm{ref}}$ such that the volume expansion near the electrode reaches a typical value of 0.2%, as observed in the experiments of LLZO volume expansion after immersion with molten Li [29]. The exact value of $c_{Li^0}^{\mathrm{ref}}$ does not alter the main conclusion of this paper, since the exponential nature of Eq. (14). Even several orders of magnitude change of this parameter only affects the location of the electron potential jump. And the stress can be calculated by generalized Hooke's law, assuming isotropic linear elasticity in small strains,

$$\boldsymbol{\sigma} = \lambda\mathrm{tr}(\boldsymbol{\varepsilon}^{\mathrm{e}})+2\mu\boldsymbol{\varepsilon}^{\mathrm{e}} \tag{15}$$

where the Lamé constants λ and μ are related to Young's modulus E and Poisson's ratio ν by $\lambda = \frac{E\nu}{(1+\nu)(1-2\nu)}$ hand $\mu = \frac{E}{2(1+\nu)}$. The stress equilibrium equation without body force can be written as,

$$\nabla\cdot\boldsymbol{\sigma} = 0 \tag{16}$$

We solved the nonlinear electro-chemo-mechanical problem by finite element method using FEniCS software [30] in Python, for both 1D and 2D cases. Again, we emphasize that due to the very deep (exponentially low) dips in electron/hole concentrations on the Brouwer diagram (two straight lines crossover on log-scale) and $t_{\mathrm{electronic}}$ minimum, the magnitude of the peak gradient when steady state is reached must be *exponentially large*, behaving like a spatial singularity front, i.e. "electrochemical shock" in our title.

3. Methods

We used FEniCS software to solve the electro-chemo-mechanical model for a domain Ω with Dirichlet boundary $\partial\Omega_1$ and Neumann boundary $\partial\Omega_2$. Since the Li ion concentration is assumed constant across the SEs, then $\widetilde{\mu}_{Li^+} = e\phi$ by definition. Then we write Eq. (9), (10) and (16) into weak forms in terms of ϕ, μ_{e^-} and $\mathbf{u}$ with Dirichlet boundary conditions $\phi^*, \mu_{e^-}^*, \mathbf{u}^*$ on $\partial\Omega_1$ and Neumann boundary conditions $\frac{\partial\phi^*}{\partial\mathbf{n}}, \frac{\partial\mu_{e^-}^*}{\partial\mathbf{n}}$

and traction $\mathbf{t}^*$ on $\partial\Omega_2$,

$$\int_\Omega \nabla\phi\cdot\nabla q dV - \int_{\partial\Omega_2} q\frac{\partial\phi^*}{\partial\mathbf{n}}dS = 0 \tag{17}$$

with $\phi = \phi^*$ on $\partial\Omega_1$

$$\int_\Omega (\sigma_{e^-}+\sigma_{h^+})\nabla(\mu_{e^-}-e\phi)\cdot\nabla q dV$$

$$-\int_{\partial\Omega_2}(\sigma_{e^-}+\sigma_{h^+})\frac{\partial(\mu_{e^-}^*-e\phi)}{\partial\mathbf{n}}dS = 0 \tag{18}$$

with $\mu_{e^-} = \mu_{e^-}^*$ on $\partial\Omega_1$

$$\int_\Omega \boldsymbol{\varepsilon}^e\cdot\mathbf{C}\cdot\nabla\mathbf{v}dV - \int_{\partial\Omega_2}\mathbf{t}^*\cdot\nabla\mathbf{v}dS = 0 \tag{19}$$

with $\mathbf{u} = \mathbf{u}^*$ on $\partial\Omega_1$

where q is trial scalar field, $\mathbf{v}$ is trial vector field, $\mathbf{n}$ is normal vector of boundary $\partial\Omega$. $\boldsymbol{\varepsilon}^e = (\nabla\mathbf{u}+\nabla\mathbf{u}^T)/2 - \boldsymbol{\varepsilon}^*$ is the elastic strain tensor, and $\mathbf{C}$ is the stiffness tensor. The above three equations are solved sequentially through Newton solver under plane stress conditions. For the 1D cases, we apply Dirichlet boundary conditions for Eqs. (17) and (18), and traction-free boundary for the mechanics problem. For 2D cases, we apply Dirichlet boundary conditions for the contact with external electrodes. When solving Eq. (18), we use the relaxation parameter of 0.1 in the Newton solver due to the high nonlinearity of the problem. The parameters used in the finite element simulations are in Table 1.

To calculate the volume expansion due to Li insertion, we conducted spin-polarized first-principles calculations by Vienna ab initio simulation package (VASP) based on density functional theory (DFT) using the projector augmented-wave (PAW) method with the Perdew-Burke-Ernzerhof (PBE) generalized gradient approximation (GGA) [32–34]. PAW potentials with 2s^1 electron for Li, 5s^{2}5p^{6}5d^{1}6s^2 for La, 4s^{2}4p^{6}4d^{2}5s^2 for Zr, 5p^{6}5d^{3}6s^2 for Ta, and 2s^{2}2p^4 electrons for O were used. The plane-wave cutoff energy was set to be 520 eV. Ta-doped Li$_7$La$_3$Zr$_2$O$_{12}$ with a cubic phase was simulated using a supercell containing 51 Li, 24 La, 11 Zr, 5 Ta, and 96 O, corresponding to a chemical composition of Li$_{6.375}$La$_3$Zr$_{1.375}$Ta$_{0.625}$O$_{12}$ that is close to Li$_{6.4}$La$_3$Zr$_{1.4-}$Ta$_{0.6}$O$_{12}$ experimentally used in the literature [35]. Compared to undoped cubic Li$_7$La$_3$Zr$_2$O$_{12}$ (crystallographic information file icsd_182312.cif [36]) that should contain 56 Li, 24 La, 16 Zr, and 96 O in the supercell with the same size, 5 substitutional Ta ions were placed randomly at the Zr sites, 23 Li ions were placed randomly at 24d sites (with a site occupancy of ~0.96), and 28 Li ions were placed randomly at 96h sites (with a site occupancy of ~0.30). Li occupations at adjacent 96h sites were excluded. To calculate reduction-induced chemical expansion, one Li atom was added to the supercell at a randomly selected 96h site (while still excluding adjacent 96h-site occupation) and three independent calculations were conducted. The Brillouin zone was sampled using Monhorst-Pack scheme with a $2\times2\times2$ $\mathbf{k}$-point mesh and convergence was considered as reached when residue atomic forces were less than 0.05 eV/Å. The volume expansion from Li insertion is listed in Table 2.

4. Results and discussion

To demonstrate the electrochemical shock introduced by the electron transport bottleneck, we simulated the one-dimensional distribution for

Table 1
Parameters for electro-chemo-mechanical model of LLZO

E (GPa)	G (GPa)	α (cm^3/mol)	$c_{Li^0}^{\mathrm{ref}}$ (mol/cm^3)
154.9 [31]	62.5 [31]	3.06	3.26×10^{-5}
$\mu_{Li^0}^{\mathrm{ref}}$(eV)	T (K)	σ_{Li^+} (S/cm)	σ_{e^-} (S/cm) at 1.48 V
1.48	300	3×10^{-4} [6]	7×10^{-20}

Table 2
DFT calculation of volume expansion from Li insertion in LLZTO

| Composition	$Li_{51}La_{24}Zr_{11}Ta_5O_{96}$	$Li_{52}La_{24}Zr_{11}Ta_5O_{96}$
Volume per supercell	2204.39 Å^3	2209.47 ± 1.43 Å^3

a single crystal LLZO with a thickness of L. As illustrated in Fig. 2a, we used the following conductivities in the Brouwer diagram: Li ion conductivity is 3×10^{-4} S cm^{-1} [6], insensitive to applied voltage; while the electron-hole conductivities are both 7×10^{-20} S cm^{-1} at 1.48 V, and change dramatically based on Eq. (11) and (12). Note the vertical axis of Fig. 2a is log-scale, thus the nature and magnitude of the electronic conductivity depend exponentially on μ_{Li^0} (a well-known feature of the Brouwer diagram), and therefore super sensitively on the δ of $Li_{7-\delta}La_3Zr_2O_{12}$, illustrating the "stiffness" of this electrochemical system. We assume this low electron-hole conductivities such that LLZO remain effectively a solid electrolyte in the voltage stability window of 0.05~2.91 V [37]. (Imagine a SSLMB requiring 1 hour to charge fully (ionic conduction), but 12 months to hold its charge (electronic leakage), this would require an electronic transference number $t_{electronic} \leqslant 10^{-4}$.) Then, a symmetrical voltage difference of 0.2 V is applied to the top and bottom boundaries, namely $\phi(x=0) = 1.58$V and $\phi(x=L) = 1.38$V. The simulated electrochemical potential of each specie is shown in Fig. 2b. The Li$^+$ electrochemical potential presents a linear profile due to the constant Li ion conductivity, while the electron and Li^0 electrochemical potential both show sharp transitions at $x = L/2$. This is

because in order to keep constant total current density, $\widetilde{\mu}_{e^-}$ requires a higher gradient to compensate for the low conductivity at $\mu_{Li^0} = 1.48$V, as demonstrated in Eq. (6). The sharp transition of $\widetilde{\mu}_{e^-}$ also leads to the potential jump of $\widetilde{\mu}_{Li^0}$, as a result of Eq. (3). Thus, the potential jumps of $\widetilde{\mu}_{e^-}$ and $\widetilde{\mu}_{Li^0}$ arise from electronic transport bottleneck even in a homogeneous electrolyte, where ionic transport bottlenecks such as grain boundaries could lead to similar potential jump effect. We also performed parametric simulations with varying potential differences across the electrolyte from 0.2 V to 0.8 V. In Fig. 2c, the distributions of Li^0 potential under different applied voltages show similar trends with abrupt potential jumps at $x = L/2$, and the magnitude of the potential jump increases with increasing applied voltage. However, the exact position of the potential jump depends sensitively on the boundary condition. If the electric potential on both boundaries increases by 1 mV, then $\widetilde{\mu}_{Li^0}$ potential drop position would shift towards the positive electrode side, demonstrated by the pink curve, and vice versa by the cyan curve. The potential gradient $\frac{\partial \widetilde{\mu}_{Li^0}}{\partial x}$ in the jump is affected by the potential difference, as shown in Fig. 2d. This gradient increases strikingly with increasing applied voltage, which could be approximated with a power law relation $\frac{\partial \widetilde{\mu}_{Li^0}}{\partial x} \propto (\Delta\phi)^n$ with $n = 4.74$. This abrupt change of $\widetilde{\mu}_{Li^0}$ will introduce a nonuniform volume expansion and internal stress field that could lead to the fracture and degradation of the SE.

Then, we tested our electro-chemo-mechanical model using a 2D problem, a rectangular SE of 3 mm × 1 mm with an electrode partially covering the top surface as shown in Fig. 3. We applied 0.24 V voltage on
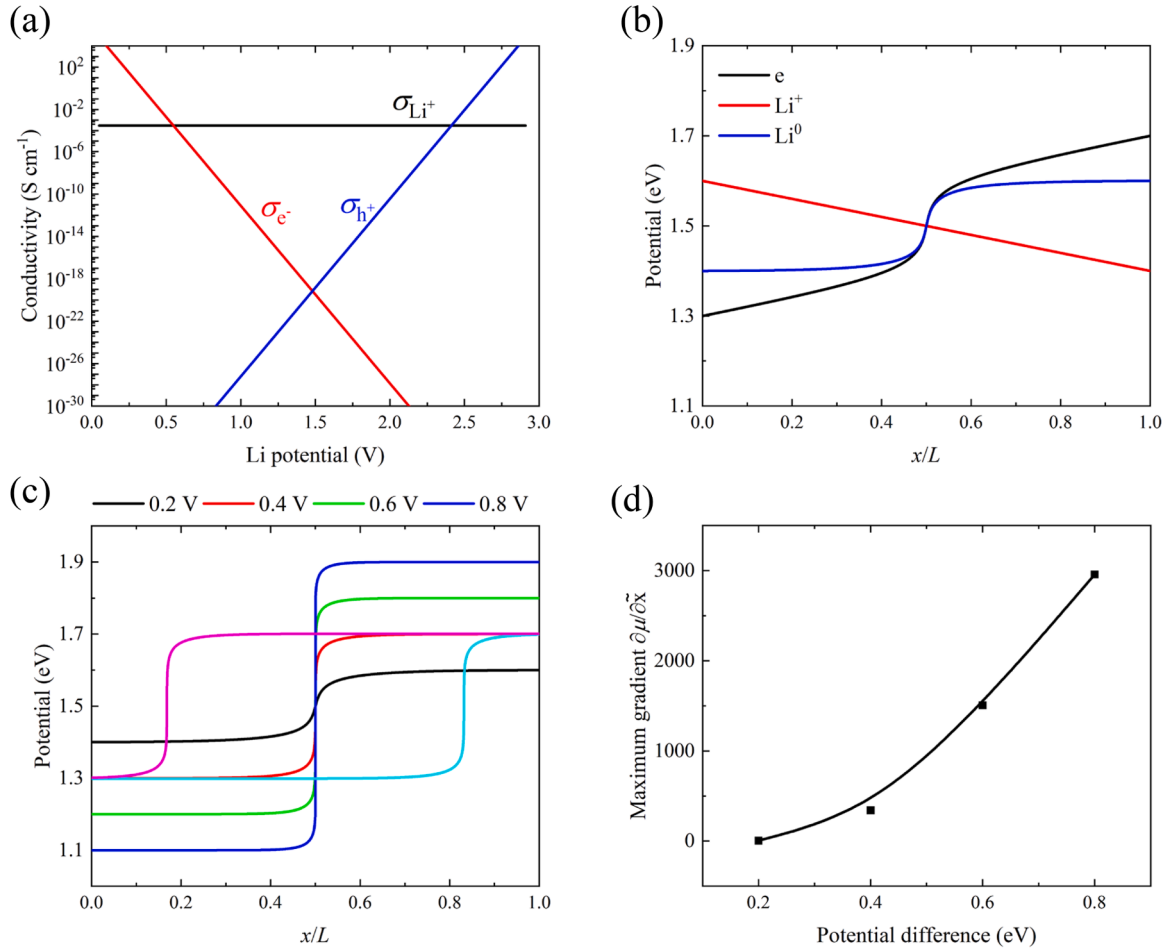
Fig. 2. Conductivity and potential distributions in 1D LLZO solid electrolyte. (a) Schematic Brouwer diagram shows redox-insensitive Li ionic conductivity and redox-sensitive electronic conductivities in LLZO. The horizontal axis of μ_{Li^0} can also be linearly mapped to the electrochemical potential U, logarithmic of the oxygen partial pressure PO_2, etc. by using the Nernst equation. (b) Distribution of electrochemical potentials of Li ions, electrons and Li^0. (c) Distribution of Li^0 potential under different applied voltage. (d) The magnitude of voltage gradient in the shock front with respect to the applied potential difference.
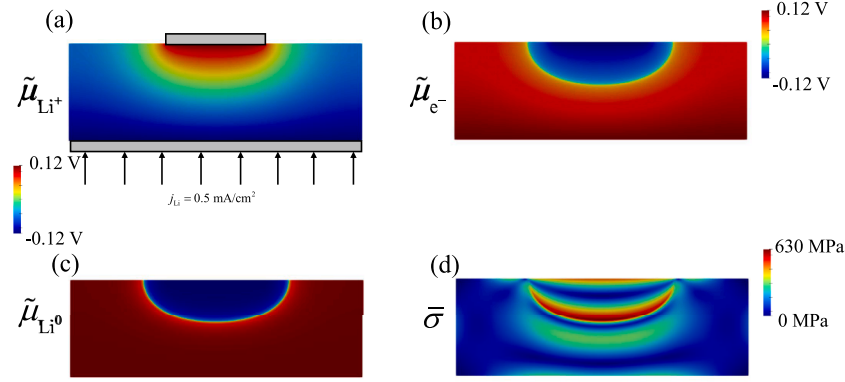
Fig. 3. The simulated electrochemical potential of Li$^+$ (a), electrons (b) and Li^0 (c) and von Mises stress field (d) in solid electrolyte LLZO. Gray rectangles represent the electrode to apply Dirichlet boundary conditions.

the SE such that the average current density across the bottom electrode reaches a typical critical current density of 0.5 mA cm^{-2} [10,11]. In Fig. 3a, the electrochemical potential of Li ion, which equals the electric potential ϕ assuming constant Li ion concentration, shows a cylindrical isosurface due to the concentrated current density from partial contact with the top electrode. In Fig. 3b and c, both the electrochemical potential of electrons $\tilde{\mu}_{e^-} \equiv -eU$ (U is directly measurable by voltmeter with respect to a reference electrode) and $\tilde{\mu}_{Li^0}$ show an abrupt potential jump inside the SE rather than the electrode-electrolyte interface, forming the bowl-shaped shock front. The potential jump of $\tilde{\mu}_{Li^0}$ is sharper than that of $\tilde{\mu}_{e^-}$, similar to the 1D case shown in Fig. 2b. According to Eq. (14), the nonuniform distribution of $\tilde{\mu}_{Li^0}$ introduces volumetric eigenstrain and internal stress field. We solved the stress equilibrium assuming the isotropic linear elasticity of the SE. The corresponding von Mises stress field is plotted in Fig. 3d. There are two high-stress regions in the SE: one is near the contacting interface, and the other one is near the bowl-shaped chemical shock front, where the eigenstrain has the highest gradient. This narrow region of transition between quite reduced LLZO and quite oxidized LLZO, forms an electrochemical shock, with a self-developed eigen-strain mismatch significant enough that can cause brittle fracture, which provides a possible explanation for the bowl-shaped crack observed in the LLZO experiment. The detailed crack initiation and propagation process warrant further studies by advanced electro-chemo-mechanical crack models with damage variable evolution.

We also utilized our electro-chemo-mechanical model to explore the optimal contact between electrodes and SE to minimize the internal stress field. In Fig. 4, we simulated several different geometries of the top electrode while keeping the total current the same, namely under the same average current density of 0.5 mA cm^{-2} [10,11] at the bottom

electrode. Fig. 4a shows the von Mises stress field of a top electrode only covering one-third of the SE top surface, generating stress as high as 630 MPa near the bowl-shaped chemical shock front demonstrated in Fig. 3c. While if we divide the top electrode into three small pieces, but with the same total contact area, as shown in Fig. 4b, the chemical shock will be more planar, therefore much lower stress with the maximum value of only 100 MPa. In Fig. 4c, we used the same number of contact points but smaller electrode sizes. Although the stress field changed quantitively, the maximum value of the stress field is still approximately 100 MPa. On the other hand, if we further increase the contacting point, the maximum stress could decrease to 85 MPa, as shown in Fig. 4d. These parametric studies show that better contact between the electrode and the SE could significantly reduce the internal stress field inside the SE. However, the stress field produced by the chemical shock cannot be erased; even uniform contact could still introduce internal stress, as shown in Fig. 2.

In addition to the electrode and SE contact, we also studied how the electronic and hole mobilities affect the internal stress field. In Fig. 5, we simulated three different scenarios, $M_{h^+}/M_{e^-} = 3/2$, $M_{h^+}/M_{e^-} = 1$ and $M_{h^+}/M_{e^-} = 2/3$. In Eq. (11) and (12), the mobilities influence the electronic and hole conductivities, controlling the relative position of red and blue curves in the Brouwer diagram in Fig. 1a. When the holes are more mobile than the electrons, the self-developed electrochemical shock and the concentrated stress region tend to move towards the positive side of the SE. In Fig. 5a and b, since the positive side of the SE is ill-contacted, the von Mises stress shows a nonuniform distribution as three connected bowl-shaped ribbons, with a maximum value of 130 MPa. Similarly, the electrochemical shock and the concentrated stress region move towards the negative side of the SE, when the electrons are more mobile than the holes, as shown in Fig. 5e and f. The volumetric
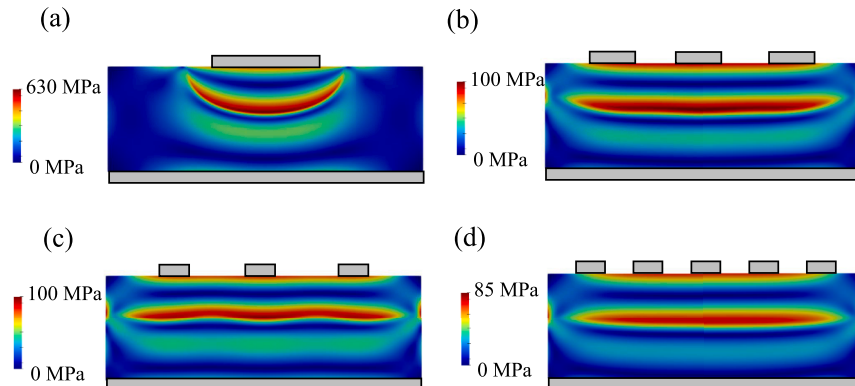
Fig. 4. Simulated von Mises stress distribution for various electrode designs under the same average current density of 0.5 mA cm^{-2} at the bottom electrode.
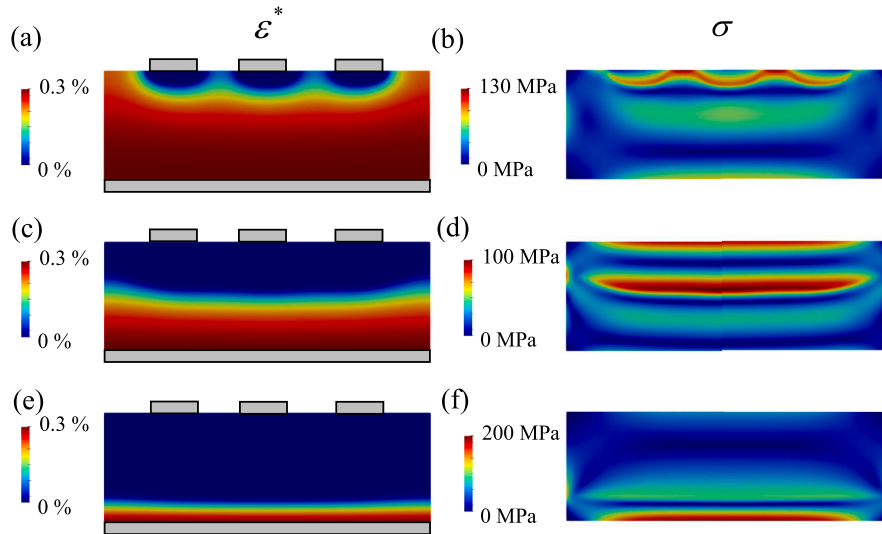
Fig. 5. Simulated volumetric eigenstrain field and von Mises stress distribution for various electrode designs under the same average current density of 0.5 mA cm^{-3} at the bottom electrode. (a,b) $M_{h^+}/M_{e^-} = 3/2$ (c,d) $M_{h^+}/M_{e^-} = 1$ (e,f) $M_{h^+}/M_{e^-} = 2/3$

eigenstrain field and von Mises stress field show planar jumps near the bottom electrode because of its perfect contact. However, the maximum value of stress reaches 200 MPa, higher than the (a,b) and (c,d). Comparing these three scenarios, the best way to minimize internal stress is to tune the relative mobilities of electrons and holes so that the potential jumps emerge in the middle of the SE rather than near any interfaces, which could be achieved by doping the SE with different elements.

5. Summary

In this paper, we proposed an electro-chemo-mechanical model to study the potential jump (exponentially large peak gradient) in the solid electrolyte limit of mixed ionic and electronic conductors. Our results lead to predictions as listed below,

(a) The electronic conductivity bottleneck $(\sigma_{e^-} + \sigma_{h^+})_{min}$ induces the sharp jump of $\widetilde{\mu}_{Li^0}$ inside the SE, not at the contacting interfaces. Despite the minute electron/hole populations and electronic conductivities $\sigma_{e^-}, \sigma_{h^+}$ in a nominally good solid electrolyte, the fact that they depend exponentially on $\widetilde{\mu}_{Li^0}$, a well-known feature of the Brouwer diagram, drives the nonlinear development, since the leaking electronic charge requires a very large driving force to maintain steady-state leakage at the spatial location of $(\sigma_{e^-} + \sigma_{h^+})_{min}$.

(b) The nature of the chemical shock is a transition zone between "reduced electrolyte" and "oxidized electrolyte" within a single electrolyte phase, that can be driven quite close to two ends of the electrochemical stability window $[\mu_{Li^0}^{lower}, \mu_{Li^0}^{upper}]$ of this solid electrolyte, depending on the voltage applied on the two terminals. When overdriven or near certain heterogeneities, it is in fact possible to locally exceed $[\mu_{Li^0}^{lower}, \mu_{Li^0}^{upper}]$ that can cause electrochemical decomposition of the solid-electrolyte single phase.

(c) The potential jump of $\widetilde{\mu}_{Li^0}$ and associated volumetric eigenstrain also generate nonuniform internal stress and provide additional thermodynamic driving forces for mechanical damage, other than Li metal (BCC) precipitation or other forms of electrochemical decomposition.

(d) The high-stress region coincides with the predicted chemical shock and potential jump. The exact location and its magnitude depend on the voltage boundary conditions, electrode geometry, contact conditions, and electron-hole mobilities of SE. These

parameters could be designed to diminish the internal stresses by our numerical model.

We have developed a comprehensive electro-chemo-mechanical framework capable of analyzing stress generation in mixed ionic electronic conductors (MIECs) under small-strain conditions. This modeling approach integrates Li-ion transport, electronic transport, and mechanical deformation phenomena. By implementing this electro-chemo-mechanical model, we conducted simulations to investigate stress generation in LLZO during the charging of a symmetrical cell. The simulation results demonstrate that various factors, including the electrode/electrolyte contact, nominal current density, electronic conductivity, and effective mass and mobilities of electrons and holes, influence the morphology of the chemical shock front and the associated stress amplitude. Notably, the simulation outcomes resemble the bowl-shaped crack observed in the in-situ scanning electron microscopy (SEM) experiment. While our study focuses specifically on LLZO, it is important to note that the proposed model can be applied generally to all MIECs, such as LiNi$_{0.8}$Co$_{0.15}$Al$_{0.05}$O$_2$, LiCoO$_2$, and LiCo$_{0.95}$Ni$_{0.05}$O$_2$, as well as certain forms of interfacial damage between MIEC/SE, MIEC/M and MIEC/MIEC.

Furthermore, by incorporating plasticity and crack propagation mechanisms, this modeling framework can be extended to investigate the functional fatigue of electrolytes and mixed conducting active electrode materials operating below the critical current density. This model has the potential to allow scientists and engineers to design SEs with custom electrode shapes and stack pressure and to detect possible hot spots for fracture. This expansion would enable a more comprehensive understanding of electrochemical system's long-term performance and durability in practical applications.

Declaration of Competing Interest

The authors declare that they have no known competing financial interests or personal relationships that could have appeared to influence the work reported in this paper.

Acknowledgments

References

[1] J.B. Goodenough, Y. Kim, Challenges for rechargeable Li batteries, Chem. Mater. 22 (3) (2010) 587–603.

[2] T. Placke, R. Kloepsch, S. Dühnen, M. Winter, Lithium ion, lithium metal, and alternative rechargeable battery technologies: the odyssey for high energy density, J. Solid State Electrochem. 21 (7) (2017) 1939–1964.

[3] M. Armand, J.M. Tarascon, Building better batteries, Nature 451 (7179) (2008) 652–657.

[4] P. Albertus, V. Anandan, C. Ban, N. Balsara, I. Belharouak, J. Buettner-Garrett, Z. Chen, C. Daniel, M. Doeff, N.J. Dudney, B. Dunn, S.J. Harris, S. Herle, E. Herbert, S. Kalnaus, J.A. Libera, D. Lu, S. Martin, B.D. McCloskey, M.T. McDowell, Y. S. Meng, J. Nanda, J. Sakamoto, E.C. Self, S. Tepavcevic, E. Wachsman, C. Wang, A. S. Westover, J. Xiao, T. Yersak, Challenges for and pathways toward Li-metal-based all-solid-state batteries, ACS Energy Lett. 6 (4) (2021) 1399–1404.

[5] J. Janek, W.G. Zeier, A solid future for battery development, Nature Energy 1 (9) (2016) 16141.

[6] R. Murugan, V. Thangadurai, W. Weppner, Fast lithium ion conduction in garnet-type Li7La3Zr2O12, Angew. Chem. Int. Ed. 46 (41) (2007) 7778–7781.

[7] C. Wang, K. Fu, S.P. Kammampata, D.W. McOwen, A.J. Samson, L. Zhang, G. T. Hitz, A.M. Nolan, E.D. Wachsman, Y. Mo, V. Thangadurai, L. Hu, Garnet-type solid-state electrolytes: materials, interfaces, and batteries, Chem. Rev. 120 (10) (2020) 4257–4300.

[8] T. Wang, J. Duan, B. Zhang, W. Luo, X. Ji, H. Xu, Y. Huang, L. Huang, Z. Song, J. Wen, C. Wang, Y. Huang, J.B. Goodenough, A self-regulated gradient interphase for dendrite-free solid-state Li batteries, Energy Environ. Sci. 15 (3) (2022) 1325–1333.

[9] A. Sharafi, H.M. Meyer, J. Nanda, J. Wolfenstein, J. Sakamoto, Characterizing the Li–Li7La3Zr2O12 interface stability and kinetics as a function of temperature and current density, J. Power Sources 302 (2016) 135–139.

[10] K. Ishiguro, Y. Nakata, M. Matsui, I. Uechi, Y. Takeda, O. Yamamoto, N. Imanishi, Stability of Nb-Doped cubic Li7La3Zr2O12 with lithium metal, J. Electrochem. Soc. 160 (10) (2013) A1690.

[11] Y. Suzuki, K. Kami, K. Watanabe, A. Watanabe, N. Saito, T. Ohnishi, K. Takada, R. Sudo, N. Imanishi, Transparent cubic garnet-type solid electrolyte of Al2O3-doped Li7La3Zr2O12, Solid State Ionics 278 (2015) 172–176.

[12] J. Qian, W.A. Henderson, W. Xu, P. Bhattacharya, M. Engelhard, O. Borodin, J.-G. Zhang, High rate and stable cycling of lithium metal anode, Nat. Commun. 6 (1) (2015) 6362.

[13] S. Hao, S.R. Daemi, T.M.M. Heenan, W. Du, C. Tan, M. Storm, C. Rau, D.J.L. Brett, P.R. Shearing, Tracking lithium penetration in solid electrolytes in 3D by in-situ synchrotron X-ray computed tomography, Nano Energy 82 (2021), 105744.

[14] Z. Ning, D.S. Jolly, G. Li, R. De Meyere, S.D. Pu, Y. Chen, J. Kasemchainan, J. Ihli, C. Gong, B. Liu, Visualizing plating-induced cracking in lithium-anode solid-electrolyte cells, Nat. Mater. 20 (8) (2021) 1121–1129.

[15] Z. Ning, G. Li, D.L.R. Melvin, Y. Chen, J. Bu, D. Spencer-Jolly, J. Liu, B. Hu, X. Gao, J. Perera, C. Gong, S.D. Pu, S. Zhang, B. Liu, G.O. Hartley, A.J. Bodey, R.I. Todd, P. S. Grant, D.E.J. Armstrong, T.J. Marrow, C.W. Monroe, P.G. Bruce, Dendrite initiation and propagation in lithium metal solid-state batteries, Nature 618 (7964) (2023) 287–293.

[16] J. Zhao, Y. Tang, Q. Dai, C. Du, Y. Zhang, D. Xue, T. Chen, J. Chen, B. Wang, J. Yao, N. Zhao, Y. Li, S. Xia, X. Guo, S.J. Harris, L. Zhang, S. Zhang, T. Zhu, J. Huang, In situ observation of Li deposition-induced cracking in garnet solid electrolytes, Energy Environ. Mater. 5 (2) (2022) 524–532.

[17] L.A. Feldman, L.C. De Jonghe, Initiation of mode I degradation in sodium-beta alumina electrolytes, J. Mater. Sci. 17 (2) (1982) 517–524.

[18] L. Porz, T. Swamy, B.W. Sheldon, D. Rettenwander, T. Frömling, H.L. Thaman, S. Berendts, R. Uecker, W.C. Carter, Y.-M. Chiang, Mechanism of lithium metal penetration through inorganic solid electrolytes, Adv. Energy Mater. 7 (20) (2017), 1701003.

[19] M. Klinsmann, F.E. Hildebrand, M. Ganser, R.M. McMeeking, Dendritic cracking in solid electrolytes driven by lithium insertion, J. Power Sources 442 (2019), 227226.

[20] S.S. Shishvan, N.A. Fleck, R.M. McMeeking, V.S. Deshpande, Dendrites as climbing dislocations in ceramic electrolytes: initiation of growth, J Power Sources 456 (2020), 227989.

[21] C.D. Fincher, D. Ojeda, Y. Zhang, G.M. Pharr, M. Pharr, Mechanical properties of metallic lithium: from nano to bulk scales, Acta Mater. 186 (2020) 215–222.

[22] Y. Dong, I.W. Chen, Oxygen potential transition in mixed conducting oxide electrolyte, Acta Mater. 156 (2018) 399–410.

[23] Y. Dong, Z. Zhang, A. Alvarez, I.W. Chen, Potential jumps at transport bottlenecks cause instability of nominally ionic solid electrolytes in electrochemical cells, Acta Mater. 199 (2020) 264–277.

[24] C. Wagner, Equations for transport in solid oxides and sulfides of transition metals, Prog. Solid State Chem. 10 (1975) 3–16.

[25] Y. Dong, H. Wang, I.W. Chen, Electrical and hydrogen reduction enhances kinetics in doped zirconia and ceria: I. grain growth study, J. Am. Ceram. Soc. 100 (3) (2017) 876–886.

[26] Y. Dong, I.W. Chen, J. Li, Transverse and longitudinal degradations in ceramic solid electrolytes, Chem. Mater. 34 (13) (2022) 5749–5765.

[27] Y. Wang, A.V. Virkar, X.-D. Zhou, On the thermodynamic origin of the formation of Li-dendrites in an electrochemical cell, J. Electrochem. Soc. 168 (10) (2021), 100503.

[28] J.H. Park, R.N. Blumenthal, Electronic transport in 8 mole percent Y2O3 - ZrO2, J. Electrochem. Soc. 136 (10) (1989) 2867.

[29] J. Wolfenstein, J.L. Allen, J. Read, J. Sakamoto, Chemical stability of cubic Li7La3Zr2O12 with molten lithium at elevated temperature, J. Mater. Sci. 48 (17) (2013) 5846–5851.

[30] M. Alnæs, J. Blechta, J. Hake, A. Johansson, B. Kehlet, A. Logg, C. Richardson, J. Ring, M.E. Rognes, G.N. Wells, The FEniCS project version 1.5, Arch. Numer. Softw. 3 (100) (2015) 9–23.

[31] S. Yu, R.D. Schmidt, R. Garcia-Mendez, E. Herbert, N.J. Dudney, J.B. Wolfenstein, J. Sakamoto, D.J. Siegel, Elastic Properties of the Solid Electrolyte Li7La3Zr2O12 (LLZO), Chem. Mater. 28 (1) (2016) 197–206.

[32] G. Kresse, D. Joubert, From ultrasoft pseudopotentials to the projector augmented-wave method, Phys. Rev. B 59 (3) (1999) 1758–1775.

[33] G. Kresse, J. Furthmüller, Efficiency of ab-initio total energy calculations for metals and semiconductors using a plane-wave basis set, Comp. Mater. Sci. 6 (1) (1996) 15–50.

[34] J.P. Perdew, K. Burke, M. Ernzerhof, Generalized Gradient Approximation Made Simple, Phys. Rev. Lett. 77 (18) (1996) 3865–3868.

[35] F. Han, A.S. Westover, J. Yue, X. Fan, F. Wang, M. Chi, D.N. Leonard, N.J. Dudney, H. Wang, C. Wang, High electronic conductivity as the origin of lithium dendrite formation within solid electrolytes, Nature Energy 4 (3) (2019) 187–196.

[36] J. Awaka, A. Takashima, K. Kataoka, N. Kijima, Y. Idemoto, J. Akimoto, Crystal structure of fast lithium-ion-conducting cubic Li7La3Zr2O12, Chem. Lett. 40 (1) (2011) 60–62.

[37] Y. Zhu, X. He, Y. Mo, Origin of outstanding stability in the lithium solid electrolyte materials: insights from thermodynamic analyses based on first-principles calculations, ACS Appl. Mater. Interfaces 7 (42) (2015) 23685–23693.